Seismicity Migration from Fluid Injection: Laboratory Experiments and Numerical Models Illuminate Volume-Driven versus Pressure-Diffusion-Driven Migration

Jun Young Song[1*], Lingfu Liu[2], Chloe Arson[2] and Gregory C. McLaskey[1]

Author information

[1] School of Civil and Environmental Engineering, Cornell University, Ithaca, NY 14850, USA; E-mail: js2795@cornell.edu (*corresponding author)

[2] Department of Earth and Atmospheric Sciences, Cornell University, Ithaca, NY 14850, USA;

Highlights

1. Teflon tape reduced diffusivity, redirected flow, and sealed the laboratory fault

2. Slow injection rate or low-viscosity fluid caused pressure-diffusion-driven migration

3. Fast injection rate or high-viscosity fluid caused volume-driven migration

Keywords

Hydraulic fracturing, Induced seismicity, Fluid injection, Seismicity migration, Laboratory experiments, Poroelastic modeling

Abstract

Fluid injection into the subsurface can induce seismicity by reactivating shear rupture, which typically produces larger earthquake magnitudes than tensile rupture. In laboratory shear rupture experiments, pressurization of the entire fault is often limited because large unconfined samples allow fluid to leak at free surfaces. In this study, we investigated shear fault reactivation by directly injecting fluid into a PMMA fault (760 mm long, 76 mm high) formed as the interface between two separate PMMA blocks. To prevent leakage in the 76 mm dimension, we made a low permeability barrier by coating the outer edges of the fault with Teflon tape. Fluid pressure then extended along the 760 mm dimension, resulting in the migration of seismicity away from the injection well. Changes in injection rate and fluid viscosity revealed two mechanisms: (1) slow injection rate or low-viscosity fluid caused seismicity migration governed by pressure diffusion, and (2) fast injection rate or high-viscosity fluid caused seismicity migration proportional to injected volume. Simulations with a 2D poroelastic model showed that seismicity migrated with the fluid pressure front in the volume-driven regime, whereas fluid pressure advanced well ahead of seismicity in the pressure-diffusion-driven regime. These results highlight that Teflon tape effectively sealed faults and controlled fluid flow, and that injection rate and fluid viscosity have a strong impact on fault slip and induced seismicity.

1. Introduction

Fluid injection into the subsurface serves a variety of geo-engineering purposes, including the disposal of large volumes of wastewater (Bao and Eaton, 2016; Keranen et al., 2014) and Carbon Capture and Storage (CCS) (Stork et al., 2015). However, such practices have been shown to elevate the risk of seismicity by reactivating faults. For example, the **M** 5.7 Prague and **M** 5.8 Pawnee earthquakes in Oklahoma, USA, were triggered by high-volume wastewater disposal (Barbour et al., 2017; Keranen et al., 2014). Beyond waste disposal, fluid injection is also employed to fracture rock (i.e., hydraulic fracturing) in applications such as Enhanced Geothermal Systems (EGS) (Majer et al., 2007) and enhanced hydrocarbon recovery (Atkinson et al., 2016; Ellsworth, 2013). Yet these operations have also been linked to induced seismicity. Notable examples include the **M** 5.5 event at Pohang (South Korea), the **M** 3.9 event at Fox creek, Alberta (Canada), the **M** 4 event at the Eagle Ford Formation, South Texas (USA), and the **M** 2.9 event at Garvin County, Oklahoma (USA) (Bao and Eaton, 2016; Fasola et al., 2019; Grigoli et al., 2018; Holland, 2013; Schultz et al., 2020). Given these risks, understanding the mechanisms of induced seismicity is crucial for mitigating potential risks to infrastructure and communities.

Fluid injection may produce tensile hydraulic fracture (Jaeger et al., 2009; Scholz, 2002) if the associated fluid pressure exceeds the tensile strength of the rock. This tensile (Mode 1) fracture typically produces only low magnitude microseismic events, often below magnitude 0 (Eaton, 2018; Eaton et al., 2018; Maxwell, 2014). Under sufficient deviatoric stress, fluid injection may significantly reduce effective normal stress. According to the Coulomb failure criterion, this stress reduction can trigger shear slip (Mode 2 and Mode 3 fractures), even without reaching tensile conditions (Jaeger et al., 2009; Scholz, 2002). Shear fractures tend to release more strain energy than tensile fracture, often resulting in larger earthquakes (Kanamori and Brodsky, 2004; Lockner, 1995).

Earthquakes associated with fluid injection are mainly attributed to pore pressure diffusion. High pressures near the injection well cause elevated pore pressure on nearby faults and fractures, which reduces the effective normal stress and reduces the resistance to shear. Pore pressure diffusion models suggest a migration of seismicity fronts for which the distance from the injection well is proportional to $\sqrt{\alpha t}$, with α and t representing hydraulic diffusivity and time, respectively (Shapiro et al., 2002, 1997). Based on this relationship, hydraulic diffusivity

has been inferred from seismic fronts, as observed in Basel (Switzerland), Soultz-sous-Forets (France), Cotton Valley (USA), Fenton hill (USA) (Mukuhira et al., 2017; Parotidis et al., 2004). Other studies noted that poroelastic stresses can also affect induced seismicity, and may be important in formations with little hydraulic connectivity (e.g. Chang and Segall, 2016; Zhai et al., 2019). Another mechanism that drives induced seismicity involves stress redistribution resulting from aseismic slip. The increased pore pressure first triggers aseismic slip, which expands outward from an injection well. As the slipping region extends beyond the area of the pressurized region, stress is transferred to adjacent locked segments, potentially triggering seismicity. This phenomenon has been observed in in-situ faults, experiments, and simulations (Bhattacharya and Viesca, 2019; Cappa et al., 2019; Guglielmi et al., 2015; Yang et al., 2023).

In laboratory studies, both tensile fractures and shear fractures have been systematically investigated to understand the mechanisms of fracture propagation and fault slip behavior under various conditions. Tensile fracture experiments have quantified fracture growth with fluid injection (Cochard et al., 2024; Ha et al., 2018; Liu et al., 2018; Yuan et al., 2024; Zhao et al., 2022), examined fracture patterns and breakdown pressure in heterogeneous layers of rocks (Teufel and Clark, 1984), and highlighted the effects of pressurization rate, viscosity of injected fluid, and cyclic injection on the breakdown pressure (Ha et al., 2018; Ishida et al., 2004; Lockner and Byerlee, 1977; Patel et al., 2017; Zoback et al., 1977). In contrast, shear fracture experiments have primarily focused on how fluids affect fault stability. For example, injection rate strongly affects slip behavior. Higher rates promote unstable slip and dynamic ruptures, while slower injection favors aseismic creep and stable sliding, thereby reducing the risk of induced seismicity (Gori et al., 2021; Ji et al., 2022; Wang et al., 2020). Fault roughness also affects slip behavior by enhancing permeability through shear dilation as asperities open faults (Ye and Ghassemi, 2018), while heterogeneous stress distributions concentrate seismic activity around asperities, leading to localized slip zones (Wang et al., 2024).

Previous shear fracture laboratory experiments have primarily been conducted on small fault samples (typically less than 100 mm in length), which may not fully capture the complexities of larger fault systems. To overcome this limitation, longer samples (e.g., ~1 m or ~3 m in length) were used for fluid injection experiments, where fluid was directly injected into the fault (Cebry et al., 2022; Cebry and McLaskey, 2021). However, the large samples have a slab-like geometry and are typically unconfined, so fluid can diffuse to a free surface of the sample

relatively close to the injection well (e.g., 38 mm diffusion distance for a 760 mm-long fault; Cebry and McLaskey, 2021). This limits the extent of pressurization along the fault and causes seismicity to occur predominantly near the injection well.

In this study, we investigated shear fracture by fluid injection, but we applied Teflon to the laboratory fault surface to reduce hydraulic diffusivity, confine the fluid, and extend the diffusion distance from 38 mm to 380 mm. The Teflon surface treatment is identical to that reported in Song and McLaskey (2024), used to modify the fault friction properties. We compared experiments with Confined Fluid (CF), where Teflon was attached along the top and bottom of the fault to produce a diffusion distance of 380 mm, to experiments with Open Fluid (OF), which has a 38 mm diffusion distance, similar to the setup in Cebry and McLaskey (2021). Both types of experiments produced several tiny seismic events. However, the CF experiments allowed fluid pressure to weaken a larger portion of the laboratory fault, and we often observed seismicity migration away from the injection well. The effects of injection rate and fluid viscosity were investigated, revealing two distinct seismic migration mechanisms: (1) pressure-diffusion-driven migration, occurring at slow injection rate or low-viscosity fluid and (2) volume-driven migration, occurring at fast injection rate or high-viscosity fluid. To better understand the mechanisms behind the migration of seismicity, a 2D numerical model was developed incorporating Darcy flow and poroelasticity. With the volume-driven regime, the fluid pressure built up faster than it diffused away, forcing the fault open and abruptly increasing the porosity and permeability of the fault zone. The resulting reduction of effective normal stress allowed the fault to slip and release stored shear strain energy as a sequence of seismic events, which migrated faster than those solely driven by pore pressure diffusion.

2. Experimental materials and methods

2.1. Experimental setup

The experiment was conducted in a biaxial machine (Cebry and McLaskey, 2021; Mclaskey and Yamashita, 2017; Song and McLaskey, 2024), with the setup illustrated in the top-view diagram (Fig. 1a). Two Polymethyl methacrylate (PMMA) blocks were used: the moving block measured 760 mm × 203 mm × 76.2 mm, while the stationary block measured 790 mm × 152 mm × 76.2 mm in the x, y, and z directions, respectively. The stationary block included 4 mm diameter injection holes drilled in it that allowed fluid to directly reach the fault plane (Fig. 1b). Normal force was applied using four hydraulic cylinders, while shear force was exerted on the moving block to induce slip along the fault plane. To minimize friction from surfaces other than the fault, Teflon sheets were inserted at the steel-to-steel (Low Friction Interface, LFI) and PMMA-to-steel interfaces. The friction coefficient of these non-fault surfaces is ~0.04 (Song et al., 2025). The end of the fault near the shear hydraulic cylinder (i.e., forcing end), is defined as the North (N) end, while the opposite end (i.e., leading end) is defined as the South (S) end.

To measure the fault slip and seismic waves, we used Eddy current sensors (square symbols) and Piezoelectric sensors (triangle symbols), respectively (Fig. 1a), attached to the sample with hot glue (Stanley, DualMelt). The Eddy current sensors, labeled E1 to E8, were positioned along the top of the block at 100 mm intervals in the x-direction. Each Eddy current sensor consisted of a probe attached to the stationary block and a steel target fixed to the moving block. Displacement of the probe relative to the target was interpreted as fault slip, recorded at 20 kHz sampling rate with a resolution of ~0.15 μm. The Piezoelectric sensors (Panametrics, V103), labeled P1 to P8, were positioned at 100 mm intervals in the x-direction and placed 40 mm away from the fault plane in y-direction. The Piezoelectric sensors were recorded continuously at 20 kHz and also at 2 MHz for 50 ms time windows when the signal exceeded the noise level.

2.2. Fault conditions

The surfaces of the PMMA blocks were fly-cut flat and then roughened using 80-grit abrasive. In the CF setup, we applied Teflon tape (Hyper Tough, 12.7 mm wide) to both sides of the fault in the (x, y) plane to prevent fluid leakage (Fig. 1c). To attach the Teflon tape to the fault, the Teflon tape was extended along the designated fault surface and fixed at both ends with adhesive tape. Before assembling the blocks, we placed plastic wrap (GLAD, Clingwrap) between the Teflon areas to prevent adhesion between them (Song and McLaskey, 2024). In

the bare PMMA region, we pre-wetted the fault with the injected fluid to ensure saturated conditions before testing. In the experimental setup by Cebry and McLaskey (2021), Talc was applied to the fault edge to induce Velocity-Strengthening (VS) behavior. To replicate similar fault conditions (an Open Fluid setup, OF), we attached Teflon, also known for its velocity-strengthening (VS) behavior (Song and McLaskey, 2024), to both ends of the faults (Fig. 1d). Comparing the CF and OF setups enabled the investigation of how the Teflon arrangement affected fluid pathways and seismicity patterns.

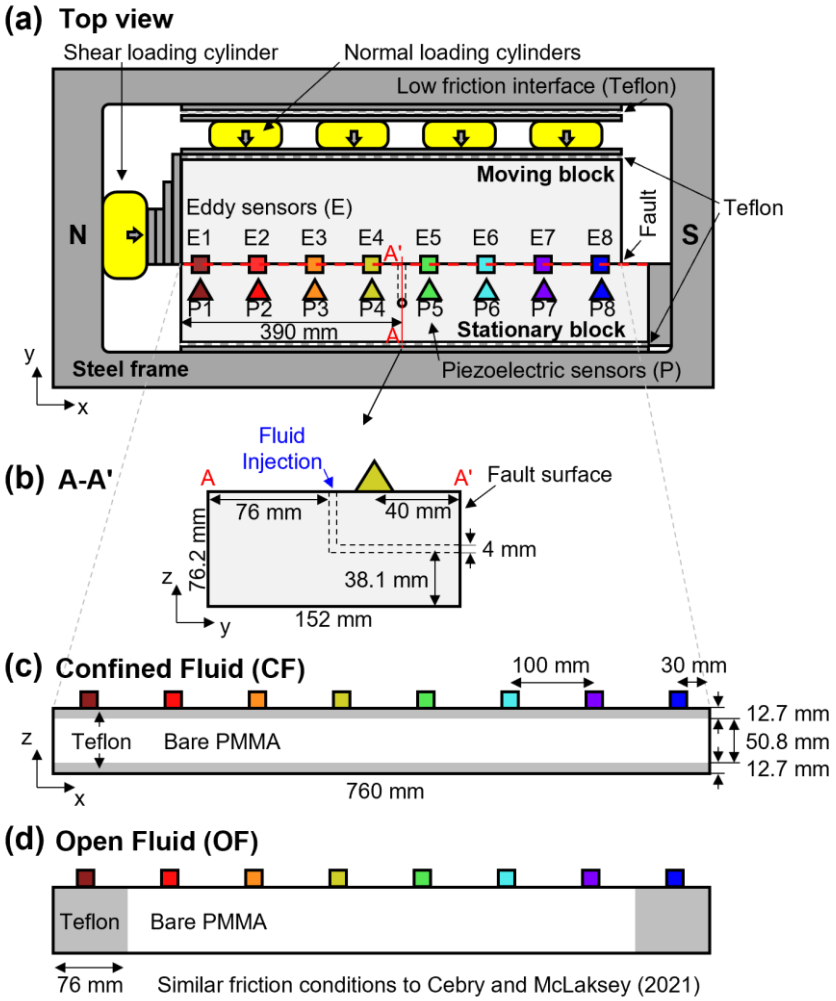

Fig. 1. (a) Top view of biaxial experimental setup. Note that 'E' and 'P' are Eddy and Piezoelectric sensors, respectively. (b) A-A' plane of stationary block for the fluid injection details. Fault conditions for (c) Confined Fluid (CF) and (d) Open Fluid (OF), which is similar to the friction conditions shown in Cebry and McLaskey (2021).

2.3. Experimental procedure

We applied a constant normal force to the x-z sample boundary which resulted in 8 MPa sample-average normal stress on the fault for all cases. We then increased the shear force on the y-z sample boundary on the moving block to produce a constant ~3 μm/s loading rate. Before conducting each experiment, we sheared the moving block by ~2 mm to avoid a run-in phase, characterized by frictional evolution with continued slip (Song and McLaskey, 2024). Once completed, we sheared the sample to generate one or two complete rupture seismic slip events (see Fig. 2a). We then paused shearing for 10 s when the sample-average shear stress on the fault reached a midpoint between the peak (τ_{peak}) and residual (τ_{res}) shear stresses (Fig. 2), after which we injected fluid according to the specified injection rates and fluid types listed in Table 1. Water (viscosity: 1 mPa·s) and a more viscous fluid (viscosity: 50 mPa·s), composed of 28 % water and 72 % glycerin (PTI Process Chemicals, Glycerin 99 %) by weight, were injected directly onto the fault surface.

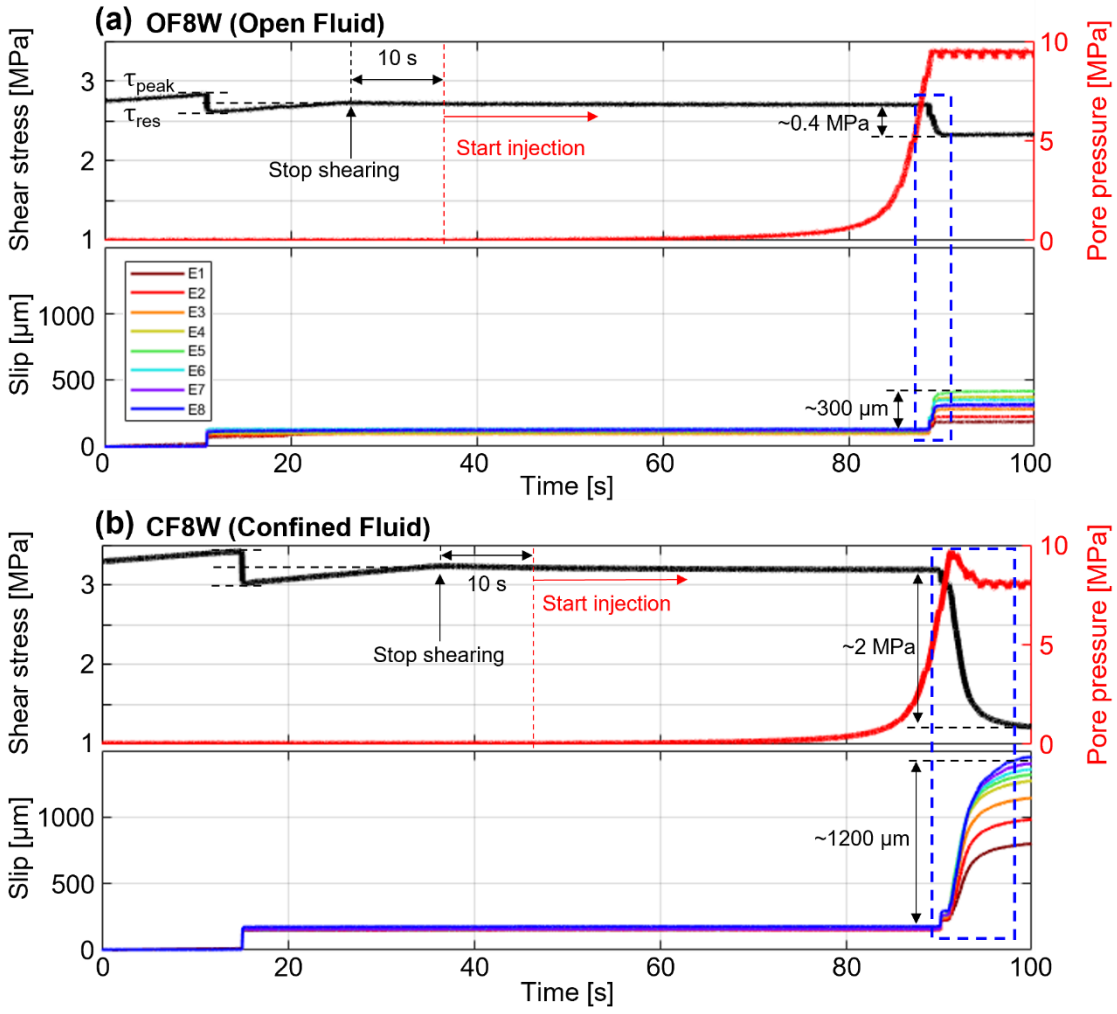

Fig. 2. Overview of sample-average shear stress, pore pressure at the injection well, and slip behavior of (a) OF8W and (b) CF8W. Shearing ceased when the sample-average shear stress reached a midpoint between the peak shear stress (τ_{peak}) and the residual shear stress (τ_{res}). Fluid injection into the fault began 8 ml/min injection rate, 10 s after stopping shearing in both tests. E1 - E8 are eight eddy current slip sensors with locations shown in Fig. 1. The region highlighted by the blue dotted area is analyzed in Fig. 3.

Table 1. Experimental conditions.

Experiment	Name	Fault condition	Injection rate [ml/min]	Injected fluid
1	OF8W	Open Fluid	8	Water
2	CF16W	Confined Fluid	16	Water
3	CF8W	Confined Fluid	8	Water
4	CF4W	Confined Fluid	4	Water
5	CF2W	Confined Fluid	2	Water
6	CF1W	Confined Fluid	1	Water
7	CF1V	Confined Fluid	1	Viscous fluid
8	CF0.5V	Confined Fluid	0.5	Viscous fluid

2.4. Hypocenter locations and magnitude of seismicity

During fluid injection onto the fault, swarms of seismic slip events were detected by Piezoelectric sensors, shown in Fig. 3. Using the recorded waveforms, we determined the hypocenter locations and estimated the moments of individual seismic slip events.

To locate the hypocenter of the seismic slip events, we used the first P-wave arrival times. Specifically, we selected the four earliest arrival times from eight sensors (P1 to P8; see Fig. S1a). An array of possible hypocenter locations was constructed along the x-direction with a spacing of 0.02 mm, covering a total length of 760 mm and resulting in 38,000 points. For each point, we computed a cost function as described below:

$$\text{Cost}(x) = \sum_{i=1}^{4} \left| (t_i - t_0) - \sqrt{(x - x_i)^2 + (y - y_i)^2 + (z - z_i)^2}/V_p \right|, \quad (1)$$

where t_i is the i^{th} Piezoelectric sensor's first arrival time and (x_i, y_i, z_i) are the i^{th} sensor's spatial coordinates, t_0 is the estimated origin time of the seismic source, and V_P is the P-wave velocity (2650 m/s for PMMA). We confine this localization to the x dimension only by assuming that the events originated near the center of the fault such that ($y - y_i$) is fixed to 40 mm, and ($z - z_i$) is fixed to 38.1 mm. The hypocenter location (x) that minimized Equation (1) was identified as the hypocenter (see Fig. S1c).

To obtain the seismic moment of the seismic slip events, we utilized the Fourier domain using the Fast Fourier Transform (FFT) algorithm. Since the recorded signals included instrument response, they were calibrated using a reference source which is a ball impact, which has been validated in previous studies (Cebry and McLaskey, 2024; McLaskey et al., 2015; Song et al., 2025; Song and McLaskey, 2024). We dropped a steel ball (~2.38 mm diameter) from a height of 0.91 m, measured the seismic signals, and calculated the equivalent seismic moment of this ball drop (M_{0_BD}) (see McLaskey et al., 2015; Song et al., 2025 for details). We then performed an FFT on the signals from all sensors and averaged the resulting spectra (Fig. S1b). To estimate the moment of the seismic slip event (M_{0_SE}), we compared the amplitude of the FFT of the seismic event to that of the ball drop event in the 4 - 9 kHz frequency range. This frequency band was chosen because it is below the corner frequency of the ball drop (~25.6 kHz; see Wu and McLaskey, 2018 for details) and still had high Signal-to-Noise Ratio (SNR) in both the ball drop and seismic event. Finally, we converted the seismic moment to magnitude (**M**) using the empirical relation (Hanks and Kanamori, 1979)

$$\mathbf{M} = 2/3 \cdot \log(M_{0\_SE}) - 6.067. \quad (2)$$

3. Experimental Results

3.1. The effect of fluid boundary condition: Open Fluid vs. Confined Fluid

The effect of the Teflon tape used to confine the fluid is examined in Fig. 2, which compares the OF8W and CF8W tests. The CF test exhibited larger shear stress reduction and slip compared to the OF test. For example, the sample-averaged shear stress in CF8W dropped by ~2 MPa, which is five times greater than the ~0.4 MPa drop observed in OF8W. The corresponding slip for CF8W reached ~1200 μm, which is four times larger than ~300 μm slip observed in OF8W. In the pore pressure evolution, the OF pressure remained stable at ~10 MPa (Fig. 2a), likely due to fluid leakage at the top and bottom of the sample, which prevented further pressure buildup (Cebry and McLaskey, 2021). In contrast, the CF test showed a pressure drop to 8 MPa (Fig. 2b), likely due to a high permeability layer by the Teflon (Section 5.3).

To analyze the seismic slip events induced by fluid injection, Fig. 3 shows a zoom in of the blue-dotted region in Fig. 2. Many seismic slip events were so small that no slip was detected with the Eddy current sensors. However, for the larger seismic slip events, we mapped the

extent of dynamic slip, defined as where the average the slip rate exceeded 3 mm/s measured using Eddy current sensors within ±0.01 s time window, surrounding the event. Figs. 3c and 3d show the extent of dynamic slip as black vertical lines. The locations of the hypocenters (circles) and their corresponding magnitudes (indicated by the color within each circle) were determined from piezoelectric sensors (see methods in Section 2.4). A representative set of signals from one seismic slip event is shown in Fig. 3e, with the earliest first arrivals detected near P4 and P5, close to the injection site. Fig. 3f shows a sequence of two seismic slip events with distinct hypocenters that occurred within a few milliseconds of each other.

In most experiments, a few small-magnitude events occurred near the injection well before the mainshock, defined as the event with the largest magnitude that ruptured the entire fault (Fig. 3c). The mainshock reduced the sample-average shear stress to τ_{res}. The main focus of this study is the migration of seismicity that occurred after the mainshock. In experiment OF8W, those events remained concentrated near the injection well, indicating that fluid pressurization and weakening were highly localized. In contrast, CF8W exhibited both a larger number of events and a more distributed rupture pattern (Fig. 3d). The hypocenters propagated bilaterally along the fault. As the hypocenters migrated, dynamic slip occurred both at the hypocenter locations and ahead of them, extending to the ends of the sample but not extending back behind the migrating front of hypocenters.

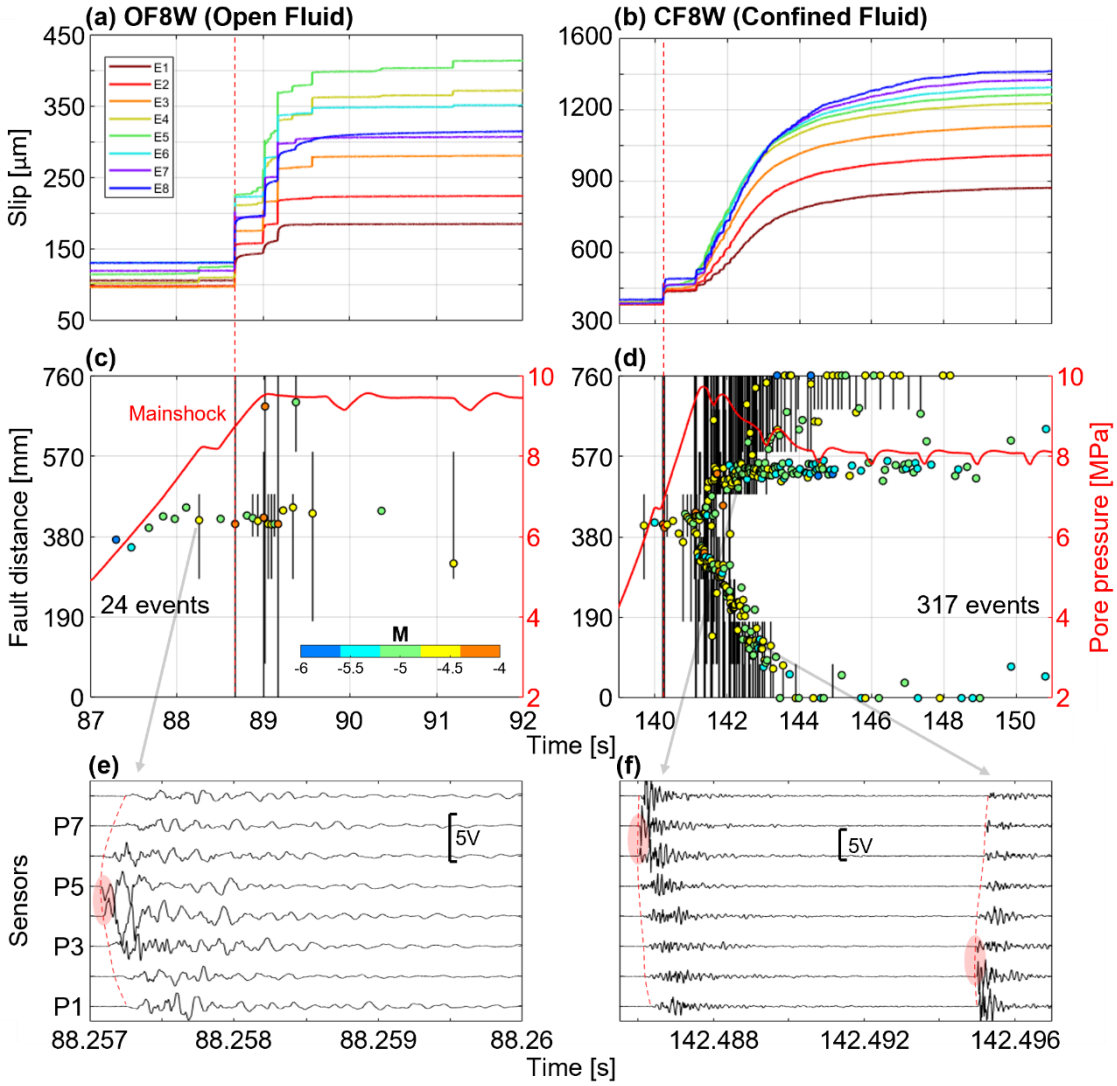

Fig. 3. Zoomed-in view of the blue dotted region in Fig. 2, highlighting fluid-induced (a) slip, (c) magnitude and hypocenter of seismicity, and (e) representative signals for OF8W, with (b), (d), and (f) showing the corresponding results for CF8W. Note that the mainshock is defined as the largest magnitude event within these slip sequences. Vertical black lines denote the extent of dynamic slip in c and d.

3.2. Effect of injection rate and fluid viscosity

Fig. 4 shows the effects of fluid injection rate and viscosity on pore pressure and seismicity for confined fault (CF) experiments. Data for other injection conditions are provided in Fig. S2. At the fast injection rate (CF16W), the mainshock occurred immediately as the first event with no detectable precursory slip (Fig. 4b), followed by seismicity that initially clustered near the injection well and then migrated outward (Fig. 4a). In contrast, the slow injection rate (CF1W) showed multiple small magnitude foreshocks near the well before the mainshock (Fig. 4c) with ~20 μm of precursory slip along most of the fault (Fig. 4d). After the mainshock, most events

remained clustered near the injection well. Some events occurred farther from the injection site, but no distinct migration was observed.

The injection of more viscous fluid (CF1V) caused a clear outward migration of hypocenters and larger event magnitudes (Fig. 4e). Despite the slow injection rate, the viscous fluid produced seismic behavior similar to that observed in fast water injection (CF16W). The mainshock resulted in ~300 μm of slip (Fig. 4f), six times more than in the water injection cases.

Table S1 summarizes the effects of loading rate and fluid viscosity. Higher injection rates of water generally produced more seismic events, larger friction drops, and higher peak pressures, but fewer foreshocks. Slow injection of viscous fluid caused larger friction changes and fewer foreshocks, similar to fast water injection (CF16W), though with fewer total events.

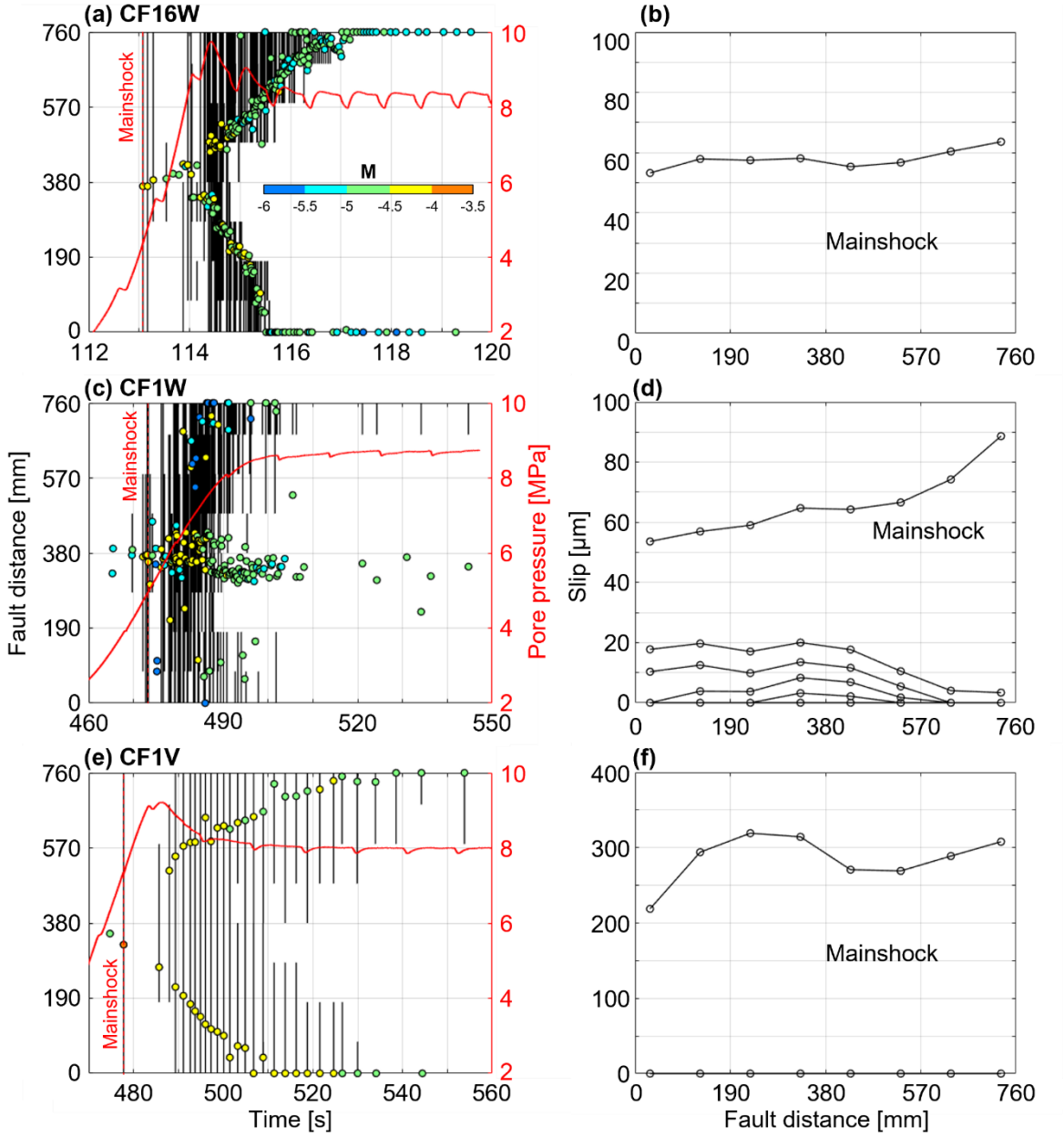

Fig. 4. Pore pressure at the injection well, along with the magnitude and hypocenter distribution of seismicity for (a) CF16W, (c) CF1W, and (e) CF1V. Cumulative slip prior to the mainshock for (b) CF16W, (d) CF1W, and (f) CF1V.

4. Numerical simulation

4.1. Model

To better understand the physical mechanisms underlying the seismicity migration, injection-driven fault dynamics were simulated using a poroelastic model implemented in the open-source Finite Element software, Multiphysics Object-Oriented Simulation Environment (MOOSE) (Permann et al., 2020). The simulation was conducted in 2D to represent the

experimental fluid injection in the x-y plane where z = 38.1 mm, corresponding to the depth of the injection well (Fig. 5a). The bulk PMMA blocks were modeled as porous media with very low porosity (10^{-4}) and permeability (10^{-6} D), while the fault was represented by a highly permeable domain of thickness 0.5 mm, in agreement with the experimental set-up. Due to the geometric symmetry of the domain, the simulations were performed on a quarter of the 2D cross-section (Fig. 5b). The open outflow boundary condition (bottom right of the simulation domain) was implemented via PorousFlowOutflowBC in MOOSE to represent the free flow through the fault outlet. With that modeling approach, fluid at the outflow boundary was removed according to the local flux derived from Darcy's law and the pressure gradient, which varied during the simulation.

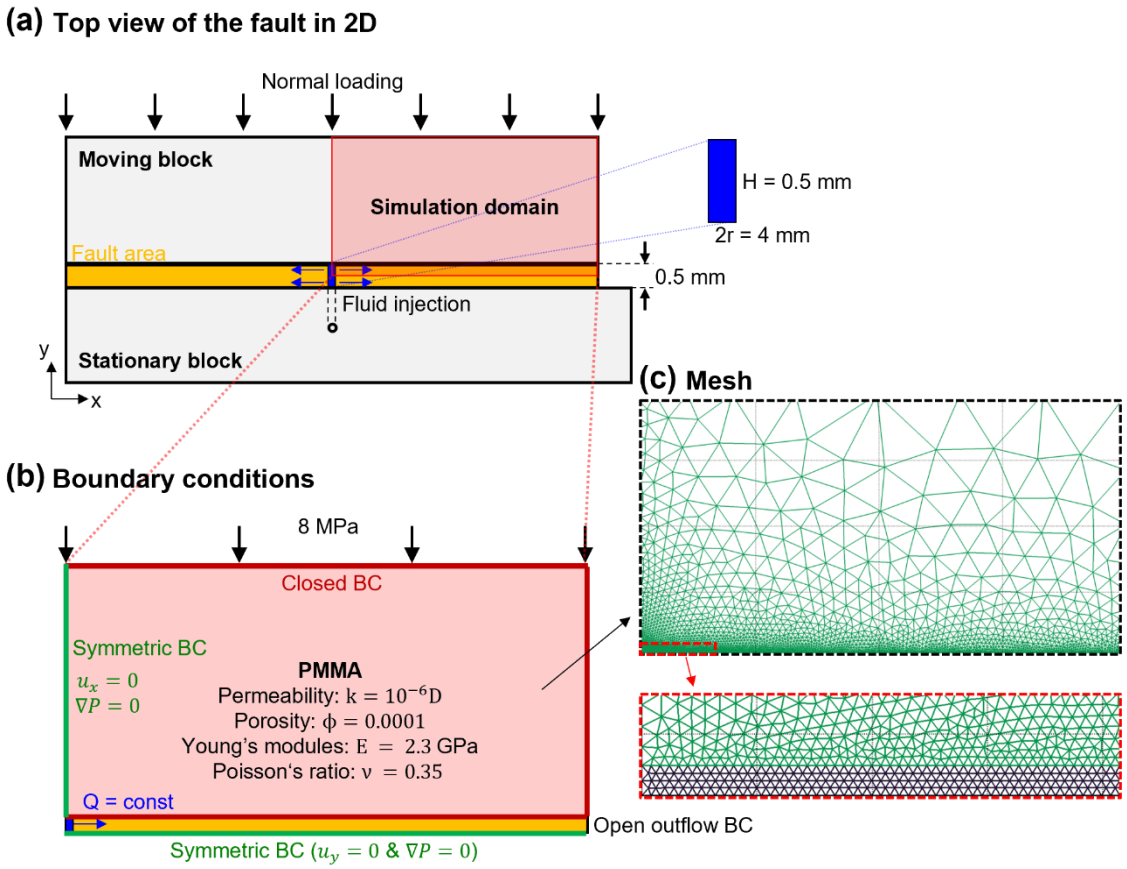

Fig. 5. (a) 2D simulation domain representing a quarter of the experimental set-up in the x-y plane at the injection position. (b) Simulation set-up with the boundary conditions (BC) and material properties employed in the numerical model. (c) Mesh adopted in the simulations, with a finer mesh in the fault region.

The PorousFlowFullySaturated action from the PorousFlow module was employed to couple fluid flow and mechanical deformation, according to the following governing equations:

$$\frac{\partial}{\partial t}(\phi\rho) + \phi\rho\nabla \cdot v_s - \nabla \cdot \left(\frac{\rho k}{\mu}\nabla P_f\right) = 0, \quad (3)$$

$$-\nabla \cdot \left(\sigma^{eff} - \alpha_B P_f I\right) = 0, \quad (4)$$

where ϕ is the porosity (dimensionless), k is the permeability (m^2 or D), ρ is the fluid density (kg/m^3), μ is the fluid dynamic viscosity (Pa·s), v_s is the velocity of the porous solid skeleton (m/s), α_B is the Biot coefficient (dimensionless, 0.8 in this study), P_f is the fluid pressure (Pa), σ^{eff} denotes the effective stress tensor (Pa), and I is the identity tensor.

Both the bulk PMMA and fault regions were considered as linear elastic porous solids (Fig. 5a). To represent fault opening without fault lateral deformation, we assigned a Poisson's ratio of 0 to the fault region. The fluid flow in both the fault and the bulk PMMA regions were assumed to follow Darcy's law. Fault aperture was modeled through porosity, which varied with fluid pressure P_f according to the following poroelastic constitutive relationship:

$$\phi = \phi^{ref} + a_P(P_f - P_f^{ref}), \quad (5)$$

where the superscript ref refers to a reference state, $a_p = 2\times10^{-7}$ Pa^{-1} to match the time scale of the fault opening dynamics observed experimentally (of the order of seconds). Additionally, we arbitrarily set $\phi^{ref} = 0.005$ to represent an initial fault porosity higher than the porosity of the PMMA blocks and P_f^{ref} = 0.1 MPa to set the reference fluid pressure equal to the atmospheric pressure. Fracture aperture can also be viewed as a linear function of fluid pressure, see for example (Ozdemirtas et al., 2009):

$$w = w^{ref} + \frac{1}{K_n}(P_f - P_f^{ref}), \quad (6)$$

where w is the fracture aperture, and K_n is the normal stiffness of the fracture. In agreement with the model described in Equation (6), in this work, fracture aperture was considered equivalent to porosity.

We assumed that fluid flow within the fault region was governed by the cubic law, such that the flow rate q could be expressed as:

$$q\ [m^2/s] = \frac{w^3}{12\mu}\nabla P_f, \quad (7)$$

$$Q\ [m^3/s] = \frac{w^3 L_z}{12\mu}\nabla P = \frac{w^2}{12}\frac{A}{\mu}\nabla P_f, \quad (8)$$

in which the area of the cross section of the flow channel is noted $A = w \cdot L_z$, where L_z is the length perpendicular to the 2D domain modeled in the simulations (i.e., z-direction in Fig. 1). Fault permeability can be seen as a quadratic function of porosity, given that $k_f = w^2/12$. Since we modeled fault opening as a porosity change, fault permeability was expressed as a function of porosity, as:

$$k_f = k_f^{open} \phi^2, \tag{9}$$

where k_f^{open} represents the permeability of the fault zone when it is fully opened (i.e., $\phi = 1$). In this work, k_f^{open} = 100 D was chosen to represent a fault with an opening w of the order of 0.1 mm, and to capture the time scale of the propagation of the fault aperture front observed experimentally. Lastly, the fluid viscosity μ was set as a value of 1 mPa·s for the water and 50 mPa·s for the viscous fluid in agreement with the experiments. The fluid density was modeled as a function of fluid pressure, as follows:

$$\rho = \rho_0 \exp\left(\frac{P_f}{K_b}\right), \tag{10}$$

where ρ_0 represents reference fluid density and K_b denotes the fluid bulk modulus.

The initial fluid pressure was set to 0.1 MPa in the entire simulation domain. The fluid was injected into the fault region as shown in Fig. 5a at various injection rates. The unit of the injection rate was converted to a mass rate per area to match the input requirements of the PorousFlowSink boundary condition in MOOSE. The injection area is the lateral surface area of the injection cylinder (shown in Fig. 5a), calculated as $2\pi \cdot r \cdot H = 2\pi \cdot (2\times10^{-3}\ m) \cdot (0.5\times10^{-3}\ m) = 2\pi\times10^{-6}\ m^2$, where r and H are the radius and height of the injection cylinder, respectively. An injection flow rate of 8 ml/min corresponds to injection volume rate per area of $1/(15\ \pi)$ $m^3/m^2/s$, which corresponds to 21 $kg/m^2/s$ for water. We varied the injection rates from 0.5 $kg/m^2/s$ to 20 $kg/m^2/s$, corresponding to volumetric injection rates ranging from 0.2 ml/min to 7.6 ml/min.

The mesh in the fault region was finer than in the bulk PMMA blocks, because of the difference of scale between the fault and bulk PMMA block zones (Fig. 5c). A first-order Lagrange interpolation was adopted for both displacement and pore pressure fields.

4.2. Distribution of porosity with different injection rates

To investigate how the injection rate of water affects the spatial distribution of porosity in the simulation, we plotted the porosity distribution along the fault distance at similar injected volumes (Fig. 6). Porosity is a function of pore pressure (Equation (5)). As pore pressure increases, porosity also increases, enhancing fluid flow within the fault. At the fastest injection rate (7.6 ml/min), porosity is higher and more localized near the injection well (Fig. 6a). In contrast, at a slower injection rate (0.5 ml/min), the porosity has lower values and is more distributed away from the injection well, even for a similar injected volume (Fig. 6b). The red dotted line at a porosity of 0.15 represents the critical porosity (ϕ_c) associated with the onset of seismicity, which is discussed in Section 5.1.2.

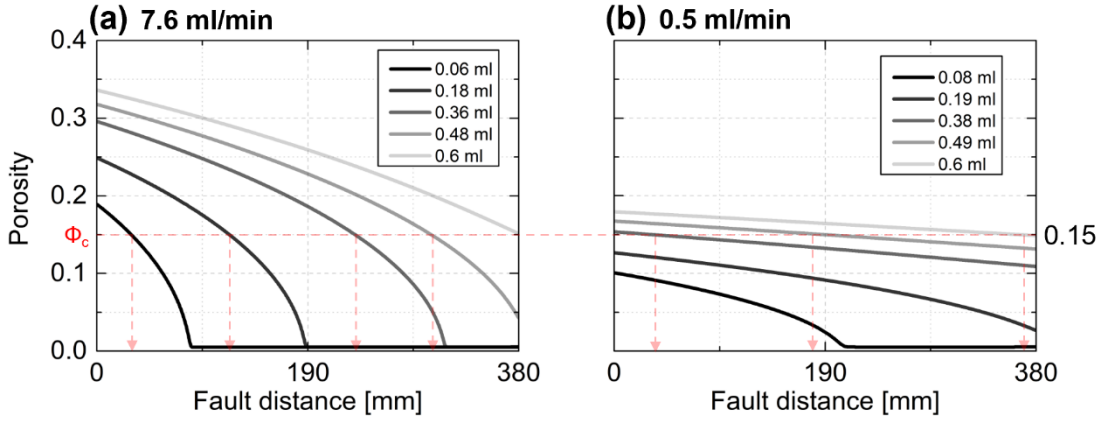

Fig. 6. Porosity distributions along the fault distance at various injected volumes of water from 0.06 ml to 0.6 ml for (a) 7.6 ml/min injection rate and (b) 0.5 ml/min injection rate. Note that ϕ_c is the critical porosity for the onset of seismicity, detailed in Section 5.1.2.

5. Discussion

Our experiments demonstrated that fault slip and seismicity patterns during fluid injection were influenced by the presence of confinement, injection rate, and fluid viscosity. The impermeable Teflon-covered fault sections used in the confined fluid (CF) experiments enhanced fault weakening by pressurizing a larger fault area compared to the open fluid (OF) experiments. Fast injection rate (e.g., CF16W) triggered an immediate mainshock without foreshocks, whereas slow injection rate (e.g., CF1W) led to a mainshock preceded by detectable slow slip and multiple associated foreshocks near the injection well. Viscous fluid injection (e.g., CF1V) produced fewer but larger magnitude seismic events, while water injection (e.g., CF1W) produced a larger number of smaller events. Results of 2D poroelastic simulations showed that at a fast injection rate, porosity increased sharply near the injection well and gradually extended along the fault, while at a slow injection rate, the porosity increase was smaller but more uniformly distributed along the fault.

5.1. Seismicity migration mechanisms

To examine the mechanisms driving seismicity migration, we first created a pressure-diffusion model that neglects poroelasticity (Section 5.1.1). While this adequately described the seismicity locations for the low injection rate, it could not explain the faster migration observed at higher injection rates and with the more viscous fluid, which we term volume-driven seismicity migration. In contrast, the experimental results could be reproduced with the poroelastic model described in Section 4 because the numerical model included fluid volume in its formulation (Section 5.1.2).

5.1.1. Pressure-diffusion model

We modeled pressure diffusion using the 2D diffusion equation:

$$\frac{\partial P_f}{\partial t} = \alpha\left(\frac{\partial^2 P_f}{\partial x^2} + \frac{\partial^2 P_f}{\partial y^2}\right), \quad (11)$$

where t is time, α (= $k_f/(\beta_c \cdot \mu)$) is the hydraulic diffusivity, and β_c is the storage coefficient. Using symmetry, we modeled 2D diffusion using only a quarter of the domain (Fig. S3a) and applied Neumann boundary conditions at the Teflon-PMMA interface and Dirichlet boundary conditions (P = 0) at the free surface at the fault end. To determine α, we used a shut-in test where fluid injection was halted at a set pressure (8 MPa, after ~40 s) and the subsequent pressure decrease over time was observed. Our analysis showed that α ranged from 8E-9 to 8E-

8 m^2/s (Fig. S3b) and no single α value could perfectly match our results, consistent with Cebry and McLaskey (2021), likely due to neglected poroelastic effects (Rutqvist and Stephansson, 2003).

Fig. 7 shows the experimental data alongside pressure contours from the pressure-diffusion modeling, (see also Figs. S3c and S3d). For the fast injection, the pressure contours barely change during the time scale of the distinct linear migration of seismicity observed at higher injection rates (Fig. 7a). Thus, the pressure-diffusion model fails to adequately explain this migration. For the slow injection rate, the hypocenters of seismicity migrated slowly and remained clustered near the contour lines, indicating that seismicity was plausibly driven by pressure diffusion (Fig. 7b).

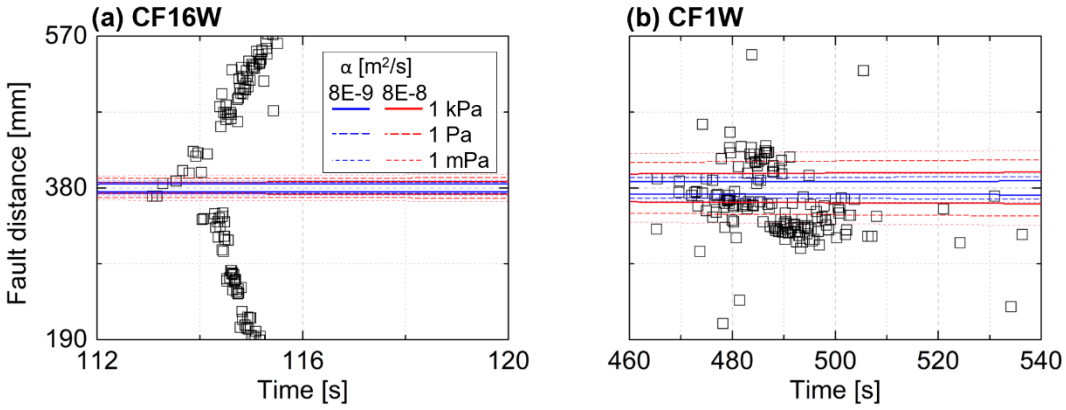

Fig. 7. Comparison of modeled pressure contours (e.g., 1 mPa, 1 Pa, and 1 kPa) for (a) CF16W and (b) CF1W. Note that pressure diffusion on fault surface is shown in Figs. S3c and S3d.

5.1.2. Seismicity migration with injected volume

To better understand the mechanism behind the migration of seismicity at fast injection rates that could not be explained by pressure diffusion, Fig. 8a shows the migration of seismicity hypocenters against injected fluid volume rather than time. The injected volume was calculated by multiplying the time and the injection rate, and the x-axis was shifted to align migration trends for comparison. When normalized this way, the propagation of seismicity in CF1V and CF16W experiments exhibit similar behavior, suggesting that injected volume played a key role. However, in CF1W, pressure appeared to be the dominant control (Fig. 7b) instead of injected volume.

To reproduce seismicity migration from the numerical simulations described in Section 4, we assumed that seismic slip events occur when the Coulomb failure criterion is reached:

$$\tau \geq \tau_{static} = \mu_{PMMA} * (\sigma_N - P_f), \quad (12)$$

where τ is the applied shear stress (set to 3.1 MPa for these experiments, see Fig. 2b), σ_N is the applied normal stress (8 MPa), and μ_{PMMA} is the static friction coefficient of PMMA, which is a tunable parameter to match with experimental results. Setting an assumed value for μ_{PMMA} produces a critical pore pressure, which corresponds to a critical value of porosity. The location of this critical porosity, ϕ_c, changes with injection volume (red dotted arrows in Fig. 6a) and its migration was used to simulate a migration of seismicity. Through trial and error, we found that ϕ_c = 0.15 matched the experimental results. That is, when normalized by the injected volume, all seismicity migration patterns collapsed to a similar form except for experiments where low-viscosity fluid was injected at a low rate (e.g., 0.5 ml/min or 0.9 ml/min injection rates) (Fig. 8b).

This ϕ_c = 0.15 corresponds to a critical pressure P_f = 0.8 MPa (Equation (5)). Combining this with the experimentally observed values of σ_N and τ, Equation (12) yields a value of μ_{PMMA} = 0.43. This falls within the previously reported range of PMMA friction coefficients, from 0.38 to 0.6 (McLaskey et al., 2012; Paglialunga et al., 2023; Wu et al., 2023).

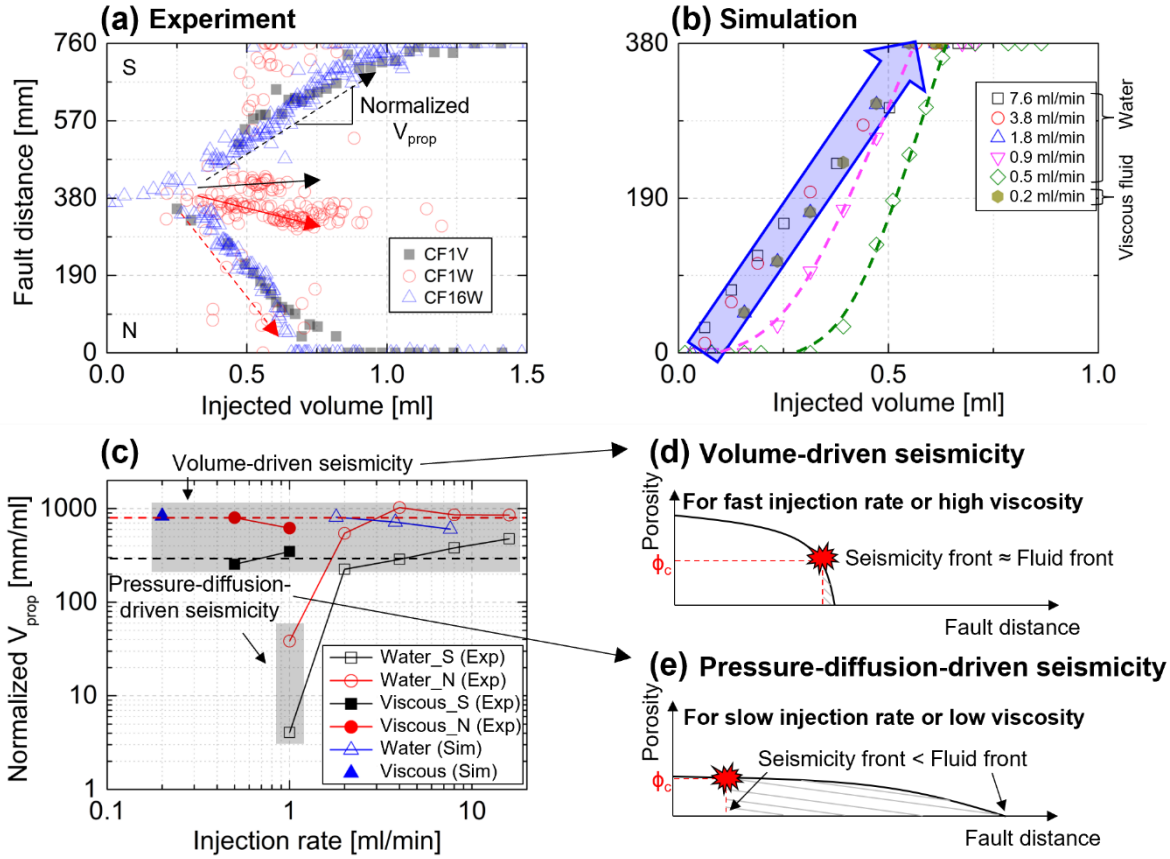

Fig. 8. (a) Migration of hypocenters as a function of injected volume in the experiment. Note that the graph has been shifted in the x-direction to align the trends for comparison. Normalized V_{prop} is defined as the fault distance divided by the injected volume. (b) Seismicity migration as a function of injected volume in the simulation. Note that each data point for fault distance corresponded to the location where the porosity distribution intersected the critical porosity. (c) Propagation velocity normalized by the injected volume of all CF fault conditions for experiment and simulation. Schematic porosity distributions for (d) volume-driven seismicity and (e) pressure-diffusion-driven seismicity (similar to Fig. 6). Note that the hashed area represents the delay in injected fluid volume between the seismicity front and fluid front.

5.1.3. Pressure-Diffusion-Driven versus Volume-Driven Seismicity Migration

To systematically study seismicity migration, Fig. 8c shows the normalized propagation velocity (V_{prop}) versus injection rate under CF fault conditions, where the velocity was calculated as the slope of fault distance versus injected volume using linear fitting (Fig. 8a). Two symbols are shown at each injection rate because seismicity migrates bilaterally and one symbol is for the N-propagating front and the other is from the S-propagating front. In nearly all the experiments, the normalized propagation velocities ranged between ~300 mm/ml and ~800 mm/ml (black and red symbols). The velocity derived from the numerical simulation was ~700 mm/ml (blue symbol), well aligned with the experimental results.

In the volume-driven seismicity migration, illustrated in Fig. 8d, fluid pressure remains concentrated near the injection point due to limited diffusion, which is characteristic of scenarios involving fast injection rate or high-viscosity fluid. The fluid pressure pushes open the fault which increases the permeability of the fault zone and enhances fluid flow. The pressure-diffusion model that lacks this poroelastic effect fails to reproduce the migration of seismicity observed experimentally (Section 5.1.1). Meanwhile, the seismicity front in the volume-driven pattern approximately matches the fluid front because of the high value and large gradient of porosity and fluid pressure. In contrast, experiment CF1W and simulations with slow injection rates and low-viscosity fluid can be described by pressure-diffusion-driven seismicity. In that regime, there is a large spatial separation between the seismicity front and the fluid front, depicted by the gray hashed region in Fig. 8e.

To further verify that the migrating seismicity closely matched the expanding fluid front, we ran an additional CF1V experiment where the fault was initially dry. The fault was pre-wetted in all previously reported experiments to ensure saturated conditions before testing; however, through the use of a dry fault, we could visually track the fluid front through the transparent PMMA (Fig. A1). Using this method, it was confirmed that the hypocenters of the seismicity generally aligned with the locations of the fluid fronts.

5.1.4. Comparison to previous work

The pressure-diffusion model cannot fully explain the volume-driven seismicity in this study. Instead, a poroelastic model that allows permeability to increase with increasing fluid pressure was needed to reproduce the seismicity migration. Yang et al. (2023) used a 2D anti-plane numerical model to confirm a direct link between the injection rate and the speed of stress transfer. They investigated the stress transfer front speed (0.01 MPa pressure contour) at high injection rates (from 3×10^5 ml/min to 6×10^6 ml/min), considering a fault opening of w = 1 m in the y-direction and a fault depth of d = 1 km in the z-direction (Fig. 1c), Within this range of injection rates, the normalized stress transfer front speed remained ~10^{-3} mm/ml. This is consistent with previous numerical simulation results showing that the slip front migration speed is proportional to the injection rate (Dublanchet, 2019; Garagash, 2021). However, at a low injection rate (1.2×10^5 ml/min), the normalized stress transfer front speed, governed by pressure diffusion, dropped to ~10^{-4} mm/ml. Despite the similarity in migration mechanism to

our experiments, the boundary injection rate between volume-driven and pressure-diffusion-driven regimes in Yang et al. (2023) is ~10^5 times higher (~2×10^5 ml/min) than in our experiments (~1.5 ml/min; Fig. 8c). This difference arises from the reservoir capacity per unit fault length: w·d is 1000 m^2 in Yang et al. (2023), whereas in our experiment, w·d is only 2.5×10^{-5} m^2 (w = 0.05 m and d = 0.0005 m; Figs. 1c and 5a). Furthermore, Yang et al. (2023) found that fluid injection-induced pore pressure triggered aseismic slip, which transferred stress to distant locked faults, causing rupture without permeability changes with pore pressure. However, the poroelastic model in this study accounts for permeability changes with pore pressure, which also affects the boundary injection rate. Finally, differences in initial model settings, such as the shear modulus of the block (0.85 GPa in this study and 32.4 GPa in Yang et al., 2023), can affect the boundary injection rate. Nevertheless, volume-driven migration of stress or seismicity is commonly observed in both stress transfer and poroelastic models.

5.2. The effect of fluid viscosity on seismicity

While fluid viscosity affects the transition between volume-driven and pressure-diffusion-driven seismicity regimes, it also appeared to affect the seismicity that was generated. Viscous fluid produced fewer seismic events, but larger magnitude events compared to water. A related observation is that with water injection, dynamic slip typically propagated from seismic hypocenters outward away from the injection well with notably no dynamic slip in regions close to the well that were already highly pressurized (Figs. 4a and 4c). In contrast, under viscous fluid injection, dynamic slip also propagated back into the region near the injection well (Fig. 4e) despite the fact that it was highly pressurized there. This observation might be explained by Cornelio and Violay (2020) who found that as fluid viscosity increased, the (a-b) parameter from the rate-and-state friction law decreased, transitioning from positive (i.e., velocity-strengthening) to negative values (i.e., velocity-weakening). This is because high-viscosity fluid leads to boundary lubrication condition, where thin fluid films coexist with solid-solid contact. This regime is highly sensitive to slip rate changes, enhancing velocity-weakening behavior as the system becomes more prone to frictional instability. Also, they found that water promoted dilation of the fault during fault slip, while viscous fluid promoted compaction, which increased pore pressure locally and reduced effective normal stress. This compaction destabilized the fault and contributed to be velocity-weakening behavior. Therefore, under viscous fluid injection, even fluid-pressurized regions adjacent to the well could experience dynamic slip, and this could be the cause of the larger magnitude events.

574

575 **5.3. High permeable pathways by Teflon tape**

576 This study showed that the Teflon technique effectively prevented fluid leakage and expanded
577 the potential applications of fluid-injection experiments in large samples that are not confined
578 within a pressure vessel. However, the Teflon tape used in this study has a thickness of ~tens
579 of microns, which created a highly permeable pathway along the edge of the bare PMMA fault
580 surface adjacent to the Teflon-covered area. This increase in permeability near the edge of the
581 Teflon can be visualized in Fig. A1 where the fluid front travels fastest near the Teflon and
582 slower in the interior of the bare PMMA region. The higher permeability pathway near the edge
583 of the Teflon region is the likely reason for the drop in fluid pressure from 10 MPa to 8 MPa
584 shown in Fig. 2b but not present in Fig. 2a. This heterogeneous permeability distribution was
585 not incorporated into the numerical simulations.

586

6. Conclusions

In this work, we investigated shear fault reactivation by directly injecting fluid into a PMMA fault (760 mm long, 76 mm high) formed from the interface between two separate blocks. To prevent leakage due to a free surface at a short distance from the injection location, we coated the section of the fault close to the free surface with Teflon tape. The enhanced weakening of the fault compared to cases without the Teflon showed that the Teflon barriers were effective at confining the fluid and enabling pressurization over a larger fault area. This Teflon confinement technique allows for more versatility in large-scale laboratory fluid injection experiments.

By varying the fluid injection rate and viscosity, two distinct migration mechanisms were observed. At slow injection rate or with low-viscosity fluid (water), seismicity slowly migrated from the injection point, termed pressure-diffusion-driven seismicity since the seismicity front followed a pressure-diffusion model. In contrast, at fast injection rate or with high-viscosity fluid, the seismicity front migrated much more rapidly, with migration rate proportional to the injected fluid volume. This migration behavior is referred to as volume-driven seismicity in this work.

A 2D poroelastic numerical model was developed, incorporating pressure-dependent permeability within the fault zone. This model reproduced the experimentally observed seismicity migration patterns by assuming that seismic events initiate when and where fluid pressure, linked to porosity (Equation (5)), reaches a critical threshold. When the experimentally applied stress levels were added to the critical fluid pressure threshold, it suggested a friction coefficient $\mu_{PMMA} = 0.43$, aligning with previously published estimates.

Overall, this study demonstrates that the migration of seismic events can be governed by either pressure diffusion or the injected volume, with the controlling mechanism determined by the injection rate, fluid viscosity, and poroelastic parameters. The volume-driven seismicity migration regime identified in this study is likely important for cases of fast injection into low permeability formations, which are conditions similar to hydraulic fracture operations for subsurface hydrocarbon operations or stimulation phases associated with enhanced geothermal systems in tight formations.

CRediT authorship contribution statement

Jun Young Song: Conceptualization, Methodology, Formal analysis, Investigation, Data curation, Validation, Writing - Original Draft, and Writing – review & editing

Lingfu Liu: Software, Methodology, Data Curation, and Writing – review & editing

Chloe Arson: Software, Methodology, Supervision, and Writing – review & editing

Gregory C. McLaskey: Conceptualization, Funding acquisition, Resources, Supervision, and Writing – review & editing.

Declaration of competing interest

The authors declare that they have no known competing financial interests or personal relationships that could have appeared to influence the work reported in this paper.

Acknowledgements

The authors gratefully acknowledge that this work was funded by National Science Foundation Grant EAR-2240375. Data reported in this paper were acquired from laboratory experiments conducted at Cornell University.

Appendix A

We conducted fluid injection under dry fault conditions, following the same procedure as in CF1V. A camera positioned beneath the fault captured high-resolution images (2640 × 1080 pixels) at 310 s, 355 s, and 370 s to compare fluid migration with seismic hypocenters. In the PMMA region, the fluid spreads out in a circular pattern (Fig. A1a). Upon reaching the boundary between the Teflon-covered and bare PMMA areas, the fluid advances more rapidly along the boundary than within the PMMA fault regions (Figs. A1b and A1c). The fluid reaches the top faster than the bottom, leading to asymmetric migration. The fluid migration region, roughly outlined in red circle, is compared with seismic hypocenters (Figs. A1d and A1e). This result indicates that the fluid front directly influences fault seismicity in volume-driven regimes (see Section 5.1.2). While many hypocenters align with fluid locations, some originate from the far end of the fault, beyond the fluid. This suggests that seismic triggering is not solely due to direct fluid injection but also influenced by other mechanisms. This may be due to stress concentration at the fault ends caused by the cessation of a previous rupture.

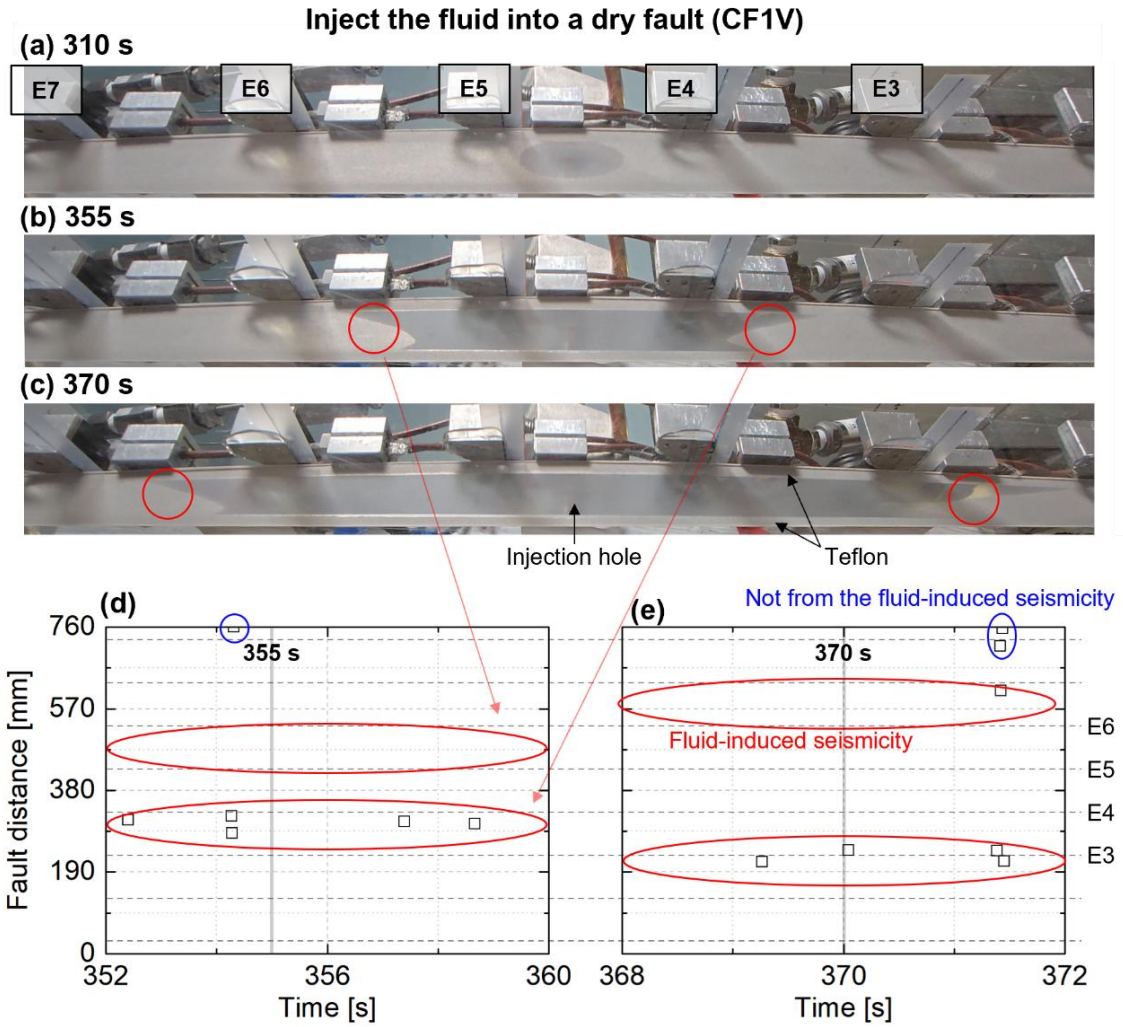

652

653 **Fig. A1. Fluid migration of CF1V under dry fault conditions at (a) 310 s, (b) 355 s, and (c)**
654 **370 s, with corresponding seismicity at (d) 355 s and (e) 370 s.**

655

656

657

References

Atkinson, G.M., Eaton, D.W., Ghofrani, H., Walker, D., Cheadle, B., Schultz, R., Shcherbakov, R., Tiampo, K., Gu, J., Harrington, R.M., Liu, Y., van der Baan, M., Kao, H., 2016. Hydraulic Fracturing and Seismicity in the Western Canada Sedimentary Basin. Seismol. Res. Lett. 87, 631–647. https://doi.org/10.1785/0220150263

Bao, X., Eaton, D.W., 2016. Fault activation by hydraulic fracturing in western Canada. Science. 354, 1406–1409. https://doi.org/10.1126/science.aag2583

Barbour, A.J., Norbeck, J.H., Rubinstein, J.L., 2017. The effects of varying injection rates in osage county, Oklahoma, on the 2016 Mw 5.8 Pawnee Earthquake. Seismol. Res. Lett. 88, 1040–1053. https://doi.org/10.1785/0220170003

Bhattacharya, P., Viesca, R.C., 2019. Fluid-induced aseismic fault slip outpaces pore-fluid migration. Science. 364, 464–468. https://doi.org/10.1126/science.aaw7354

Cappa, F., Scuderi, M.M., Collettini, C., Guglielmi, Y., Avouac, J.P., 2019. Stabilization of fault slip by fluid injection in the laboratory and in situ. Sci. Adv. 5, 1–8. https://doi.org/10.1126/sciadv.aau4065

Cebry, S.B.L., Ke, C.Y., McLaskey, G.C., 2022. The Role of Background Stress State in Fluid-Induced Aseismic Slip and Dynamic Rupture on a 3-m Laboratory Fault. J. Geophys. Res. Solid Earth 127, 1–19. https://doi.org/10.1029/2022JB024371

Cebry, S.B.L., McLaskey, G.C., 2024. Heterogeneous high frequency seismic radiation from complex ruptures. Seismica 3. https://doi.org/10.26443/seismica.v3i2.1351

Cebry, S.B.L., McLaskey, G.C., 2021. Seismic swarms produced by rapid fluid injection into a low permeability laboratory fault. Earth Planet. Sci. Lett. 557, 116726. https://doi.org/10.1016/j.epsl.2020.116726

Chang, K.W., Segall, P., 2016. Injection-induced seismicity on basement faults including poroelastic stressing. J. Geophys. Res. Solid Earth 121, 2708–2726. https://doi.org/10.1002/2015JB012561

Cochard, T., Svetlizky, I., Albertini, G., Viesca, R.C., Rubinstein, S.M., Spaepen, F., Yuan, C., Denolle, M., Song, Y.-Q., Xiao, L., Weitz, D.A., 2024. Propagation of extended fractures by local nucleation and rapid transverse expansion of crack-front distortion. Nat. Phys. 20, 660–665. https://doi.org/10.1038/s41567-023-02365-0

Cornelio, C., Violay, M., 2020. Effect of Fluid Viscosity on Earthquake Nucleation. Geophys. Res. Lett. 47, 1–9. https://doi.org/10.1029/2020GL087854

Dublanchet, P., 2019. Fluid driven shear cracks on a strengthening rate-and-state frictional fault. J. Mech. Phys. Solids 132, 103672. https://doi.org/10.1016/j.jmps.2019.07.015

Eaton, D.W., 2018. Passive Seismic Monitoring of Induced Seismicity. Cambridge University Press. https://doi.org/10.1017/9781316535547

Eaton, D.W., Igonin, N., Poulin, A., Weir, R., Zhang, H., Pellegrino, S., Rodriguez, G., 2018. Induced Seismicity Characterization during Hydraulic-Fracture Monitoring with a Shallow-Wellbore Geophone Array and Broadband Sensors. Seismol. Res. Lett. 89, 1641–1651. https://doi.org/10.1785/0220180055

698 Ellsworth, W.L., 2013. Injection-Induced Earthquakes. Science. 341, 1–7.
699 https://doi.org/10.1126/science.1225942

700 Fasola, S.L., Brudzinski, M.R., Skoumal, R.J., Langenkamp, T., Currie, B.S., Smart, K.J., 2019.
701 Hydraulic Fracture Injection Strategy Influences the Probability of Earthquakes in the
702 Eagle Ford Shale Play of South Texas. Geophys. Res. Lett. 46, 12958–12967.
703 https://doi.org/10.1029/2019GL085167

704 Garagash, D.I., 2021. Fracture mechanics of rate-and-state faults and fluid injection induced
705 slip. Philos. Trans. R. Soc. A Math. Phys. Eng. Sci. 379, 20200129.
706 https://doi.org/10.1098/rsta.2020.0129

707 Gori, M., Rubino, V., Rosakis, A.J., Lapusta, N., 2021. Dynamic rupture initiation and
708 propagation in a fluid-injection laboratory setup with diagnostics across multiple temporal
709 scales. Proc. Natl. Acad. Sci. 118. https://doi.org/10.1073/pnas.2023433118

710 Grigoli, F., Cesca, S., Rinaldi, A.P., Manconi, A., López-Comino, J.A., Clinton, J.F.,
711 Westaway, R., Cauzzi, C., Dahm, T., Wiemer, S., 2018. The November 2017 M w 5.5
712 Pohang earthquake: A possible case of induced seismicity in South Korea. Science. 360,
713 1003–1006. https://doi.org/10.1126/science.aat2010

714 Guglielmi, Y., Cappa, F., Avouac, J.P., Henry, P., Elsworth, D., 2015. Seismicity triggered by
715 fluid injection-induced aseismic slip. Science. 348, 1224–1226.
716 https://doi.org/10.1126/science.aab0476

717 Ha, S.J., Choo, J., Yun, T.S., 2018. Liquid CO2 Fracturing: Effect of Fluid Permeation on the
718 Breakdown Pressure and Cracking Behavior. Rock Mech. Rock Eng. 51, 3407–3420.
719 https://doi.org/10.1007/s00603-018-1542-x

720 Hanks, T.C., Kanamori, H., 1979. A moment magnitude scale. J. Geophys. Res. B Solid Earth
721 84, 2348–2350. https://doi.org/10.1029/JB084iB05p02348

722 Holland, A.A., 2013. Earthquakes Triggered by Hydraulic Fracturing in South-Central
723 Oklahoma. Bull. Seismol. Soc. Am. 103, 1784–1792.
724 https://doi.org/10.1785/0120120109

725 Ishida, T., Chen, Q., Mizuta, Y., Roegiers, J.-C., 2004. Influence of Fluid Viscosity on the
726 Hydraulic Fracturing Mechanism. J. Energy Resour. Technol. 126, 190–200.
727 https://doi.org/10.1115/1.1791651

728 Jaeger, J.C., Cook, N.G.W., Zimmerman, R., 2009. Fundamentals of Rock Mechanics. John
729 Wiley & Sons.

730 Ji, Y., Wang, L., Hofmann, H., Kwiatek, G., Dresen, G., 2022. High-Rate Fluid Injection
731 Reduces the Nucleation Length of Laboratory Earthquakes on Critically Stressed Faults
732 in Granite. Geophys. Res. Lett. 49, 1–13. https://doi.org/10.1029/2022GL100418

733 Kanamori, H., Brodsky, E.E., 2004. The physics of earthquakes. Reports Prog. Phys. 67, 1429–
734 1496. https://doi.org/10.1088/0034-4885/67/8/R03

735 Keranen, K.M., Weingarten, M., Abers, G.A., Bekins, B.A., Ge, S., 2014. Sharp increase in
736 central Oklahoma seismicity since 2008 induced by massive wastewater injection.
737 Science. 345, 448–451. https://doi.org/10.1126/science.1255802

738 Liu, P., Ju, Y., Gao, F., Ranjith, P.G., Zhang, Q., 2018. CT Identification and Fractal

Characterization of 3-D Propagation and Distribution of Hydrofracturing Cracks in Low-Permeability Heterogeneous Rocks. J. Geophys. Res. Solid Earth 123, 2156–2173. https://doi.org/10.1002/2017JB015048

Lockner, D., Byerlee, J.D., 1977. Hydrofracture in Weber Sandstone at high confining pressure and differential stress. J. Geophys. Res. 82, 2018–2026. https://doi.org/10.1029/JB082i014p02018

Lockner, D.A., 1995. Rock Failure, in: A Handbook of Physical Constants. pp. 127–147. https://doi.org/10.1029/RF003p0127

Majer, E.L., Baria, R., Stark, M., Oates, S., Bommer, J., Smith, B., Asanuma, H., 2007. Induced seismicity associated with Enhanced Geothermal Systems. Geothermics 36, 185–222. https://doi.org/10.1016/j.geothermics.2007.03.003

Maxwell, S., 2014. Microseismic Imaging of Hydraulic Fracturing. Society of Exploration Geophysicists. https://doi.org/10.1190/1.9781560803164

McLaskey, G.C., Lockner, D.A., Kilgore, B.D., Beeler, N.M., 2015. A Robust Calibration Technique for Acoustic Emission Systems Based on Momentum Transfer from a Ball Drop. Bull. Seismol. Soc. Am. 105, 257–271. https://doi.org/10.1785/0120140170

McLaskey, G.C., Thomas, A.M., Glaser, S.D., Nadeau, R.M., 2012. Fault healing promotes high-frequency earthquakes in laboratory experiments and on natural faults. Nature 491, 101–104. https://doi.org/10.1038/nature11512

Mclaskey, G.C., Yamashita, F., 2017. Slow and fast ruptures on a laboratory fault controlled by loading characteristics. J. Geophys. Res. Solid Earth 122, 3719–3738. https://doi.org/10.1002/2016JB013681

Mukuhira, Y., Dinske, C., Asanuma, H., Ito, T., Häring, M.O., 2017. Pore pressure behavior at the shut-in phase and causality of large induced seismicity at Basel, Switzerland. J. Geophys. Res. Solid Earth 122, 411–435. https://doi.org/10.1002/2016JB013338

Ozdemirtas, M., Babadagli, T., Kuru, E., 2009. Experimental and Numerical Investigations of Borehole Ballooning in Rough Fractures. SPE Drill. Complet. 24, 256–265. https://doi.org/10.2118/110121-PA

Paglialunga, F., Passelègue, F., Latour, S., Gounon, A., Violay, M., 2023. Influence of Viscous Lubricant on Nucleation and Propagation of Frictional Ruptures. J. Geophys. Res. Solid Earth 128, 1–16. https://doi.org/10.1029/2022JB026090

Parotidis, M., Shapiro, S.A., Rothert, E., 2004. Back front of seismicity induced after termination of borehole fluid injection. Geophys. Res. Lett. 31, 1–5. https://doi.org/10.1029/2003GL018987

Patel, S.M., Sondergeld, C.H., Rai, C.S., 2017. Laboratory studies of hydraulic fracturing by cyclic injection. Int. J. Rock Mech. Min. Sci. 95, 8–15. https://doi.org/10.1016/j.ijrmms.2017.03.008

Permann, C.J., Gaston, D.R., Andrš, D., Carlsen, R.W., Kong, F., Lindsay, A.D., Miller, J.M., Peterson, J.W., Slaughter, A.E., Stogner, R.H., Martineau, R.C., 2020. MOOSE: Enabling massively parallel multiphysics simulation. SoftwareX 11, 100430. https://doi.org/10.1016/j.softx.2020.100430

Rutqvist, J., Stephansson, O., 2003. The role of hydromechanical coupling in fractured rock engineering. Hydrogeol. J. 11, 7–40. https://doi.org/10.1007/s10040-002-0241-5

Scholz, C.H., 2002. The Mechanics of Earthquakes and Faulting. Cambridge University Press. https://doi.org/10.1017/CBO9780511818516

Schultz, R., Skoumal, R.J., Brudzinski, M.R., Eaton, D., Baptie, B., Ellsworth, W., 2020. Hydraulic Fracturing-Induced Seismicity. Rev. Geophys. 58, 1–43. https://doi.org/10.1029/2019RG000695

Shapiro, S.A., Huenges, E., Borm, G., 1997. Estimating the crust permeability from fluid-injection-induced seismic emission at the KTB site. Geophys. J. Int. 131, F15–F18. https://doi.org/10.1111/j.1365-246X.1997.tb01215.x

Shapiro, S.A., Rothert, E., Rath, V., Rindschwentner, J., 2002. Characterization of fluid transport properties of reservoirs using induced microseismicity. Geophysics 67, 212–220. https://doi.org/10.1190/1.1451597

Song, J.Y., Cattania, C., McLaskey, G., 2025. Fault healing and asperity partitioning on a frictionally heterogeneous laboratory fault. https://doi.org/10.22541/essoar.174886019.99803345/v1

Song, J.Y., McLaskey, G.C., 2024. Laboratory Earthquake Ruptures Contained by Velocity Strengthening Fault Patches. J. Geophys. Res. Solid Earth 129, 1–16. https://doi.org/10.1029/2023JB028509

Stork, A.L., Verdon, J.P., Kendall, J.M., 2015. The microseismic response at the In Salah Carbon Capture and Storage (CCS) site. Int. J. Greenh. Gas Control 32, 159–171. https://doi.org/10.1016/j.ijggc.2014.11.014

Teufel, L.W., Clark, J.A., 1984. Hydraulic Fracture Propagation in Layered Rock: Experimental Studies of Fracture Containment. Soc. Pet. Eng. J. 24, 19–32. https://doi.org/10.2118/9878-PA

Wang, L., Kwiatek, G., Renard, F., Guérin-Marthe, S., Rybacki, E., Bohnhoff, M., Naumann, M., Dresen, G., 2024. Fault roughness controls injection-induced seismicity. Proc. Natl. Acad. Sci. 121, 2017. https://doi.org/10.1073/pnas.2310039121

Wang, L., Kwiatek, G., Rybacki, E., Bonnelye, A., Bohnhoff, M., Dresen, G., 2020. Laboratory Study on Fluid-Induced Fault Slip Behavior: The Role of Fluid Pressurization Rate. Geophys. Res. Lett. 47, 1–12. https://doi.org/10.1029/2019GL086627

Wu, B.S., McLaskey, G.C., 2018. Broadband Calibration of Acoustic Emission and Ultrasonic Sensors from Generalized Ray Theory and Finite Element Models. J. Nondestruct. Eval. 37, 1–16. https://doi.org/10.1007/s10921-018-0462-8

Wu, G., Zhang, K., Wang, C., Li, X., 2023. Nucleation Mechanism and Rupture Dynamics of Laboratory Earthquakes at Different Loading Rates. Appl. Sci. 13, 12243. https://doi.org/10.3390/app132212243

Yang, Y., Yang, H., Zi, J., 2023. Stress transfer outpaces injection-induced aseismic slip and triggers seismicity. Sci. Rep. 13, 1–12. https://doi.org/10.1038/s41598-023-43760-0

Ye, Z., Ghassemi, A., 2018. Injection-Induced Shear Slip and Permeability Enhancement in Granite Fractures. J. Geophys. Res. Solid Earth 123, 9009–9032.

https://doi.org/10.1029/2018JB016045

Yuan, C., Cochard, T., Denolle, M., Gomberg, J., Wech, A., Xiao, L., Weitz, D., 2024. Laboratory Hydrofractures as Analogs to Tectonic Tremors. AGU Adv. 5, 1–15. https://doi.org/10.1029/2023AV001002

Zhai, G., Shirzaei, M., Manga, M., Chen, X., 2019. Pore-pressure diffusion, enhanced by poroelastic stresses, controls induced seismicity in Oklahoma. Proc. Natl. Acad. Sci. 116, 16228–16233. https://doi.org/10.1073/pnas.1819225116

Zhao, Y., Zhang, Y., Yang, H., Liu, Q., Tian, G., 2022. Experimental study on relationship between fracture propagation and pumping parameters under constant pressure injection conditions. Fuel 307, 121789. https://doi.org/10.1016/j.fuel.2021.121789

Zoback, M.D., Rummel, F., Jung, R., Raleigh, C.B., 1977. Laboratory hydraulic fracturing experiments in intact and pre-fractured rock. Int. J. Rock Mech. Min. Sci. Geomech. Abstr. 14, 49–58. https://doi.org/10.1016/0148-9062(77)90196-6

Supplementary Material for:

Seismicity Migration from Fluid Injection: Laboratory Experiments and Numerical Models Illuminate Volume-Driven versus Pressure-Diffusion-Driven Migration

Jun Young Song[1*], Lingfu Liu[2], Chloe Arson[2] and Gregory C. McLaskey[1]

Author information

[1] School of Civil and Environmental Engineering, Cornell University, Ithaca, NY 14850, USA; E-mail: js2795@cornell.edu (*corresponding author)

[2] Department of Earth and Atmospheric Sciences, Cornell University, Ithaca, NY 14850, USA;

Contents of this File:

Figures S1-S3

Table S1

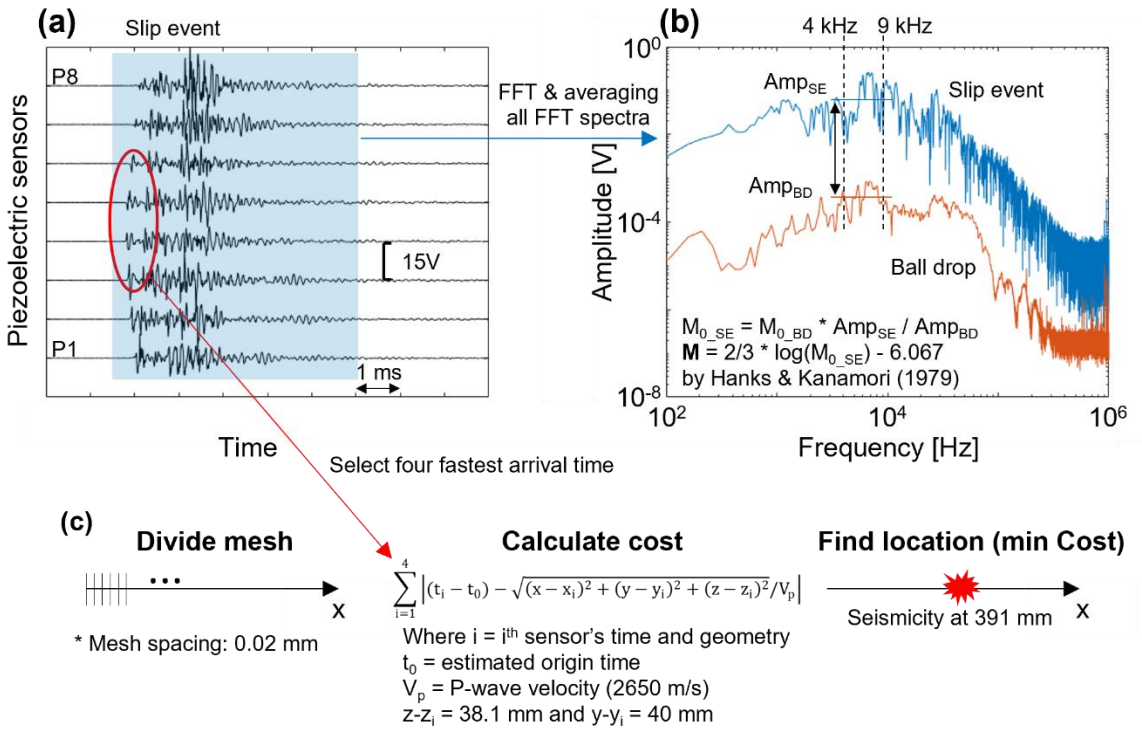

Fig. S1. (a) Representative signals from the slip event in time domain and (b) averaged frequency-domain spectra (via FFT) for both the ball drop and slip event. (c) Process for determining the seismic event location in one-dimensional analysis: divide the mesh for calculation, compute the cost function at each mesh point, and identify the minimum cost, which corresponds to the seismic event location. Note that the four fastest arrival signals were used for the cost calculation.

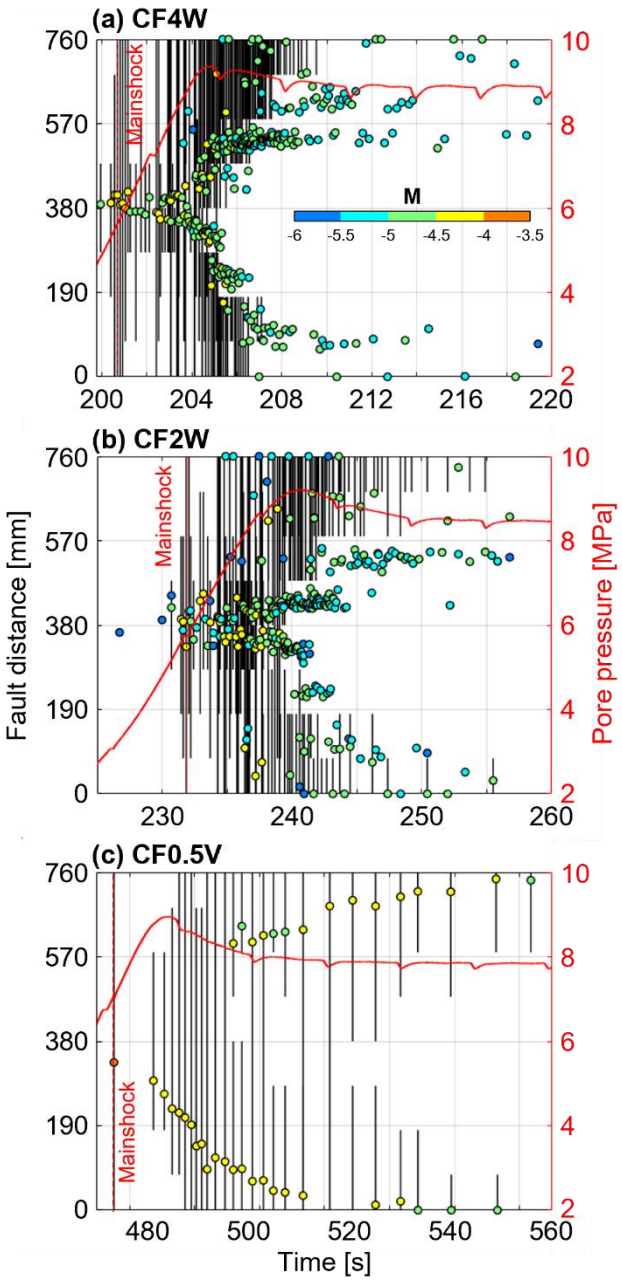

Fig. S2. Pore pressure at the injection well, along with the magnitude and hypocenter distribution of seismicity for (a) CF4W, (b) CF2W, and (c) CF0.5V.

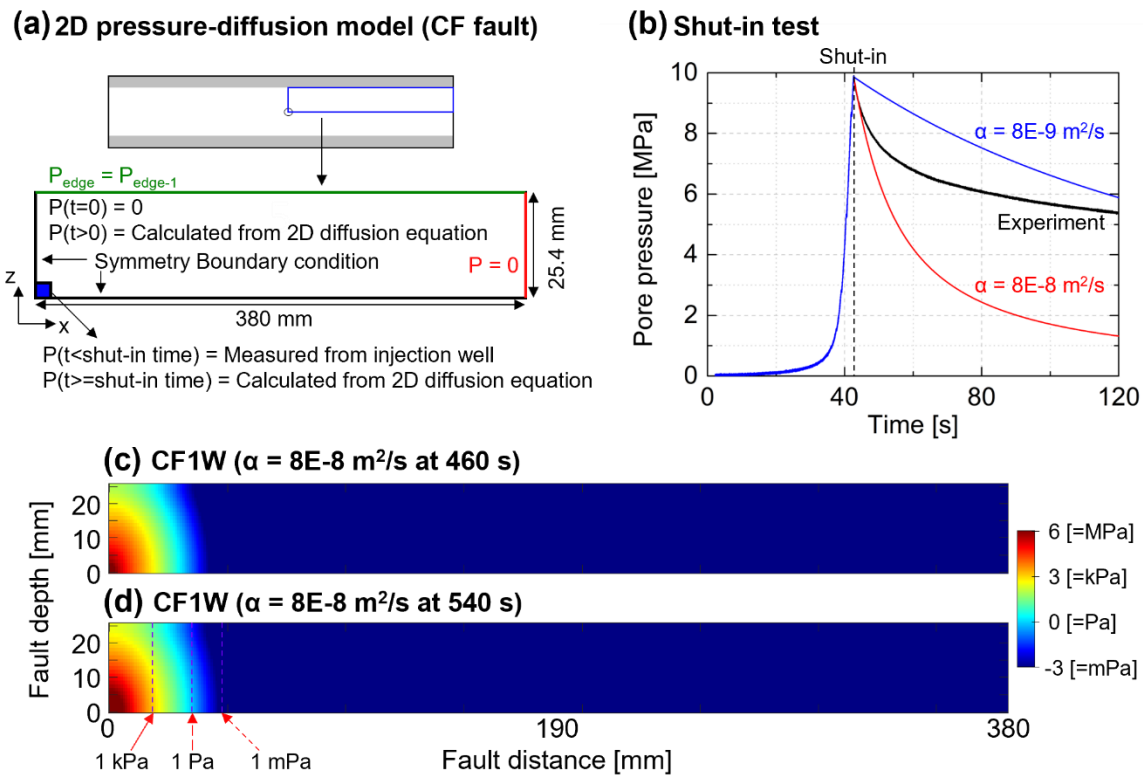

Fig. S3. (a) Schematic 2D pressure-diffusion model with boundary conditions. (b) Shut-in test to obtain the range of the hydraulic diffusion coefficient in CF fault condition. Note that water injection continued until ~40 s before being stopped. Pressure distribution with distance for CF1W using water for α = 8e-8 m²/s at (c) 460 s and (d) 540 s. Note that the color scale represents pressure on a logarithmic scale.

Table S1. Mechanical properties with different loading rates and viscosities. Note that friction coefficient is the ratio of sample-average shear and normal stresses.

Exp	Total events [Count]	Foreshocks [Count]	Peak fluid pressure [MPa]	Change of friction coefficient
CF16W	274	0	9.7	0.25
CF8W	317	2	9.7	0.24
CF4W	314	3	9.4	0.23
CF2W	288	7	9.2	0.22
CF1W	190	7	8.6	0.19
CF1V	53	1	9.2	0.21
CF0.5V	39	0	9.0	0.15